RSC Sustainability

Accepted Manuscript

This article can be cited before page numbers have been issued, to do this please use: N. Minh Quang, D. M. Nguyen, V. C. N. C. N. ANH, D. Tuan, T. T. Tam Toan and A. Dao, *RSC Sustainability*, 2026, DOI: 10.1039/D6SU00059B.

View Article Online
DOI: 10.1039/D6SU00059B

Sustainability Spotlight Statement

This work addresses the critical need for rapid, on-site monitoring of antibiotic residues (ceftriaxone) in livestock to prevent food chain contamination and antimicrobial resistance. Traditional detection methods like HPLC are resource-intensive and reliant on toxic organic solvents. To solve this, a green electrochemical sensor based on WS_2–RGO heterostructures was developed via a reagent-free hydrothermal assembly, eliminating the use of hazardous reducing agents typical in graphene synthesis. Furthermore, the optimization process employed Chemometrics (Box–Behnken Design), significantly reducing experimental trials, energy consumption, and chemical waste compared to conventional optimization. This study provides a sustainable, cost-effective, and field-deployable analytical tool, aligning directly with UN SDG 3 (Good Health and Well-being) and SDG 12 (Responsible Consumption and Production) by ensuring safer food supply chains through resource-efficient technologies.

Facile Hydrothermal Assembly of WS_2–RGO Heterostructures Guided by Chemometrics: A Green Electrochemical Strategy for Ceftriaxone Surveillance in Livestock

View Article Online
DOI: 10.1039/D6SU00059B

Nguyen Minh Quang[a], Do Mai Nguyen[b], Vo Chau Ngoc Anh[c], Dinh Tuan[d]

Tran Thanh Tam Toan[e,*], Anh Quang Dao [f,g,*]

[a]Faculty of Chemical Engineering, Industrial University of Ho Chi Minh City, Ho Chi Minh City, 700000, Vietnam

[b]University of Sciences, Hue University, Hue city, 530000, Vietnam

[c]University of Medicine and Pharmacy, Hue University, 530000, Vietnam

[d]Nam Can Tho University, Can Tho 900000, Vietnam

[e]Dong A University, Danang city, 550000, Vietnam

[f] Faculty of Environmental and Natural Sciences, Duy Tan University, Da Nang, 550000, Viet Nam

[g]Institute of Research and Development, Duy Tan University, Da Nang, 550000, Viet Nam

Corresponding Authors:

* *daoanhquang@duytan.edu.vn (A.Q. Dao)*

* *tranthanhtamtoan@gmail.com (T.T.T. Toan)*

Abstract

The development of high-performance nanomaterials for electrochemical sensing is critical for ensuring food safety and public health. This work presents the fabrication and optimization of a Tungsten Disulfide–Reduced Graphene Oxide (WS_2–RGO) heterostructure for the sensitive voltammetric detection of ceftriaxone (CEF), an antibiotic of significant epidemiological relevance. The composite material was synthesized via a facile hydrothermal route, with structural characterization confirming the successful anchoring of WS_2 nanosheets onto the conductive RGO scaffold. To maximize analytical performance, a Box–Behnken Design (BBD) combined with Response Surface Methodology (RSM) was employed to optimize the experimental parameters. The optimized WS_2–RGO/GCE sensor exhibited remarkable current amplification and enhanced electron-transfer kinetics for CEF oxidation, offering a wide linear range (0.02–12.8 μM) and a low limit of detection (LOD) (0.009 μM). The method was successfully validated in swine urine samples, achieving

satisfactory recovery (rev) rates (96.8%–103.8%) and demonstrating statistical agreement with HPLC (high-performance liquid chromatography). Driven by a facile, green-synthesis approach, this study provides a robust, cost-effective, and field-amenable solution for rapid surveillance of antibiotic residues in the livestock supply chain.

View Article Online
DOI: 10.1039/D5SU00959B

Keywords: Micro/nano interfacial mechanics, WS_2–RGO heterostructure electrode, Box–Behnken design (RSM), Ceftriaxone sensing, Voltammetric method

Introduction

Third-generation cephalosporins, typified by ceftriaxone, have been prioritized by global health agencies because of their critical role in treating severe human infections and the elevated public health risk posed by resistance to this class. Their non-human use has therefore been urged to be minimized under the WHO Medically Important Antimicrobials framework and recent updates to stewardship guidance [1,2]. In parallel, food-animal production systems have been shown to be vulnerable to antimicrobial overuse and the consequential occurrence of drug residues in the human food chain. National monitoring in Vietnam has detected antimicrobial residues in retail meats (e.g., 4.1% of pork samples), underscoring the need for rapid residue surveillance alongside traditional laboratory methods [3]. Concurrently, a pressing public-health concern has emerged in Hue City, Central Vietnam, where clusters of *Streptococcus suis* infections have been epidemiologically linked to the consumption of pork products [4]. This zoonotic risk necessitates intensified prophylactic antimicrobial protocols in local husbandry, which, if uncontrolled, significantly elevates the probability of antibiotic residues—such as ceftriaxone—entering the food chain [5]. Consequently, the development of sensitive, field-amenable analytical tools is urgently required to screen for these residues at slaughter and retail sites, addressing a critical gap in the current rapid surveillance infrastructure.

Electrochemical sensing is increasingly adopted for antibiotic analysis due to its high sensitivity, fast readout, and operational field amenability. Compared with established techniques such as HPLC, MS, or spectrophotometry, electrochemical measurements offer practical benefits, including inexpensive instrumentation, portability, and minimal sample preparation [6]. In addition, electrode-surface engineering allows selectivity and sensitivity to be tuned, making these methods well-suited for the targeted determination of analytes such as ceftriaxone. For ceftriaxone, voltammetric assays have been reported at bare glassy-carbon electrodes (GCEs) and

View Article Online
DOI: 10.1039/D5SU00059B

at nanocarbon-modified GCEs, and progressively lower detection limits have been achieved using designs such as Pt–CNT composites, MOF/β-cyclodextrin coatings, and custom screen-printed platforms [7–10].

While surface modification is frequently employed to mitigate electrode fouling by phenolic compounds, its primary utility in ceftriaxone sensing lies in amplifying the electroactive surface area (Aeff) and accelerating interfacial electron-transfer kinetics (k^o). The incorporation of nanostructured modifiers reduces the charge transfer resistance (R_{ct}) at the electrode-electrolyte interface, thereby enhancing the sensitivity towards the target analyte [11]. Furthermore, the stability of the modified interface in the measurement medium is critical for maintaining reproducible analytical signals over repeated scans, ensuring that the sensor performance is governed by defined electrochemical parameters rather than random surface fluctuations [11,12].

A wide spectrum of nanostructures with new compositions and architectures has been reported, broadening the options for nanomaterial (NMTs)-based sensors [13–26]. Recent studies indicate that carbon nanofibers [27] and multi-walled carbon nanotubes [11] could be used to determine parabens. Nevertheless, depositing these materials onto the detecting electrodes typically involves multi-step fabrication or the incorporation of noble-metal components, resulting in interfaces with strong anti-fouling behavior. It has led to broad research dedicated to optimizing physicochemical characteristics, morphologies, and dimensions of NMTs so that laboratory concepts better align with practical requirements. In addition, in terms of market analysis, to detect an analyte at a higher temperature, often relies on micro-heater assemblies, which increase cost, power consumption, and footprint and may shorten lifetime because of the merging of grain boundaries of nanostructures operated at high temperature [10,28–30]. While Reduced Graphene Oxide (RGO) is a well-established material in energy storage and electronics, its specific application as a conductive scaffold for Tungsten Disulfide (WS_2) in the electrochemical sensing of cephalosporin antibiotics remains comparatively underutilized in the context of food safety monitoring [31,32].

In recent years, electrodes incorporating RGO have gained broad attention as transducers because RGO combines high electrical transport, specific surface area and operational stability under electrochemical conditions, attributes valued in sensing and energy-storage devices. RGO is obtained by reducing graphene oxide, a process that removes a portion of the oxygen functionalities and partly restores the π-

View Article Online
DOI: 10.1039/D6SU00059B

conjugated network. The recovery of conductivity, together with defects/edge sites created during reduction, provides additional electroactive centers, improving interfacial reaction kinetics [33–36].

When compared with graphene oxide (GO)—which is largely insulating owing to abundant hydroxyl, epoxide, and carboxyl groups—RGO exhibits much higher conductivity after reduction. Consequently, RGO-modified electrodes generally show faster electron transfer, greater analytical sensitivity, and enhanced voltammetric responses across sensing applications. These transport advantages make RGO a suitable scaffold for electrochemical sensors in which rapid charge transfer governs analytical performance [37,38].

To improve analytical figures of merit further, two-dimensional (2D) heterostructures that couple high-conductivity carbon scaffolds with catalytically active transition-metal dichalcogenides (TMDCs) have been leveraged [39,40]. Reduced graphene oxide (RGO) provides a high surface area and efficient electron-transport network, while WS_2 supplies abundant edge-site chemistry and favorable band energetics for redox mediation. Heterostructured WS_2–graphene hybrids have therefore been shown to enhance charge transfer, increase electroactive surface area, and amplify sensing responses across diverse targets [41,42]. Interface engineering of TMDC/graphene composites has further been reported to optimize catalytic pathways and suppress recombination losses, which are advantageous for trace-level electroanalysis [43].

Under increasing emphasis on computationally informed design at micro- and nano-structured interfaces, multivariate experimental planning was adopted so that the search for operating conditions would be posed as a numerical optimization problem rather than an ad-hoc parameter sweep. Response surface methodology (RSM) was originally formulated to approximate complex response–factor relationships by low-order polynomials and to guide sequential experimentation toward stationary points with statistical control, providing a principled alternative to one-factor-at-a-time tuning. The classical formulation and its modern developments have established the routine use of second-order models, lack-of-fit diagnostics, and prediction-oriented variance analysis in method optimization [44–46].

Within the RSM family, the Box–Behnken design (BBD) has been favored for electroanalytical method development because full quadratic surfaces are estimated using three factor levels while avoiding extreme “corner” combinations. Such

View Article Online
DOI: 10.1039/D6SU00059B

geometry is advantageous for micro/nano-engineered electrodes where over-polarization or surface restructuring may occur at factor extremes. The original Technometrics article introduced this three-level second-order class, and comparative assessments in analytical chemistry have documented its run economy, near-rotatability, and uniform prediction precision relative to central composite and three-level factorial designs [45]. In practice, waveform and preconcentration variables (e.g., accumulation potential and time, and pulse parameters) are efficiently interrogated, weak interactions are quantified, and curvature is resolved without excessive experimental burden, key requirements when interfacial kinetics and mass transport co-evolve at reduced scales [47].

For β-lactam antibiotics, statistically designed multivariate optimization has already been shown to improve voltammetric determination. In the case of ceftriaxone, factorial, RSM workflows have been used to tune nano-enabled carbon/metal interfaces and to resolve the analyte in the presence of interferents, underscoring the practical value of design-of-experiments in this analyte class [10]. Complementary advances in disposable micro/nano-structured electrodes further indicate that materials engineering and numerical optimization act synergistically to elevate sensitivity and robustness in ceftriaxone sensing [48]. Against this backdrop, a BBD-based RSM strategy is employed here to (i) construct a statistically adequate quadratic surrogate for the ceftriaxone peak current, (ii) diagnose model adequacy via ANOVA and lack-of-fit tests, and (iii) navigate the design landscape by contour and ridge analyses before experimental verification. When multiple analytical figures of merit must be balanced, desirability-function optimization provides a standard, transparent route to a single compromise operating point, and is naturally compatible with the RSM framework adopted [49]. This integration of data-efficient numerical optimization with micro/nano-interface design aligns with current priorities in computation-assisted mechanics and manufacturing of materials at reduced scales, while setting up the subsequent sections that report the optimized conditions and analytical validation.

While electrochemical sensing of ceftriaxone has been established, the specific application of 2D TMDC/graphene heterostructures for its detection remains limited, particularly in terms of validation in complex porcine matrices. This work addresses the immediate need for field-amenable tools to monitor residues associated with *Streptococcus suis* transmission risks. Consequently, sensitive, low-cost monitoring of ceftriaxone is urgently required. Against this backdrop, a WS_2–RGO-modified glassy

View Article Online
DOI: 10.1039/D5SU00059B

carbon electrode is proposed, which enhances interfacial charge transfer and significantly amplifies the voltammetric response to ceftriaxone—thereby delivering a clear methodological advance that addresses an immediate regional public health need. To achieve this, the present study systematically investigates and optimizes key operational parameters, specifically the medium pH, accumulation potential (E_{acc}), accumulation time (t_{acc}), and pulse amplitude (ΔE), to maximize the analytical sensitivity.

Experimental

Chemicals

Sodium hydroxide (or NaOH, ≥ 98%), nitric acid (or HNO_3, ≥ 98%), acetic acid (CH_3COOH, ≥ 98%), boric acid (H_3BO_3, ≥ 98%), phosphoric acid (H_3PO_4, ≥ 97%), potassium hydroxide (KOH, ≥ 98%), ceftriaxone and reduced graphene oxide (RGO) were purchased from Merck supplier (Germany nation). Sodium tungstate dihydrate ($Na_2WO_4.2H_2O$, ≥ 99%, Xilong city), thiourea (CH_4N_2S, 99%, Shanghai, China), hydroxylammonium chloride ($HONH_3Cl$, ≥ 98.5%, Xilong, China), *N*-cetyl-*N*,*N*,*N*-trimethylammonium bromide or CTAB ($C_{19}H_{42}BrN$, 98%, HiMEDIA supplier, India). Britton-Robinson buffer (or BRBS) was obtained by 0.55 M CH_3COOH, 0.5 M H_3BO_3, and 0.55 M H_3PO_4. The desired pH buffer was made by using 1.2 M KOH or 1.2 M H_3PO_4 solutions.

Instruments

Raman spectra were reported on XploRA, HORIBA (Japan), with a 532 nm YAG Laser. Scanning electron microscopy (SEM) images were acquired using SEM JMS-5300LV (Japan). Energy Dispersive X-ray (EDX)-elemental maps were acquired with a Horiba EMAX ENERGY EX-400 system (Japan). The specific surface area was calculated by the Brunauer–Emmett–Teller (BET) model, and the mesoporous surface area was measured by the t-plot method.

Voltammetry was carried out on a Computerized Polarography Analyzer CPA-HH5 potentiostat using a conventional three-electrode cell consisting of a glassy carbon electrode GCE, an Ag/AgCl 3 M KCl reference (RE-5, BAS), and a platinum-wire counter electrode.

HPLC (high performance liquid chromatography) high analyses were performed on a Thermo Ultimate 3000 system with UV–Vis detector (λ = 275 nm). A C18 (250 × 4 mm; 5 μm) chromatographic column was employed. The column oven was

maintained at 45.2 ± 1.0 °C, the mobile phase was delivered at 2.0 mL min^{-1}, and 10 µL injections were used with a volume is 5 mL. Quantification was performed using an external-standard approach based on chromatographic peak areas.

Synthesis of WS_2-RGO

A precursor mixture containing 1.7 g $Na_2WO_4.2H_2O$, 1.4 g CH_4N_2S, and 0.7 g $NH_2OH.HCl$ was added to 30 mL of deionized water under stirring. Next, 0.3 g CTAB was introduced and the suspension was stirred for 1 h; a white precipitate formed and the pH was measured at 6. 1 g of RGO was then incorporated and the mixture was stirred for another 1 h. The product was transferred to a 50 mL Teflon-lined autoclave and heated at 180 °C for 24 h. After natural cooling, the solids were filtered, washed with deionized water, and dried at 80 °C for 24 h [50–52].

Preparation of WS_2-RGO/GCE

The GCE was polished with Al_2O_3 (0.05 µm), followed by cleaning in 1:2 (*v*/*v*) HNO_3 and rinsing twice with deionized water. Additional cleaning was performed by ultrasonication in an ethanol/water (1:1, *v*/*v*) bath. The electrode was then air-dried with a tungsten-filament heater at 40 °C.

WS_2–RGO (10 mg) was dispersed in 10 mL deionized water and sonicated for ~24 h. To 1.0 mL of the 1 mg mL^{-1} dispersion, 50 µL of 0.1 % Nafion (in ethanol) was added to obtain a homogeneous ink (denoted solution A). Nafion acted as the binder for film formation [28]. The GCE was modified by drop-casting 10 µL of solution A onto the surface and allowing it to dry at room temperature. The resulting WS_2–RGO/GCE was used as the working electrode in subsequent measurements.

Box-Behnken Design and Response Surface Model

In this study, to place the voltammetric study on a systematic footing and to ensure continuity with the pH selection, a response surface methodology (RSM) campaign was undertaken to maximize the anodic peak current (*Ip*) of ceftriaxone (CEF) at the WS_2–RGO/GCE while keeping the physicochemical context fixed (BRBS, pH 5) for subsequent analytical evaluation. Three instrumental factors were optimized: accumulation potential (E_{acc}, x), accumulation time (t_{acc}, y), and pulse amplitude (ΔE, z). The experiment list, coding scheme, and data treatment followed the Box–Behnken design (BBD) prepared in Minitab and executed in randomized order; 12 edge points and 3 center replicates (total N = 15) were used to fit a second-order polynomial. The experimental run size was determined from the Box–Behnken relation [53]

$$N = 2k(k-1) + C_o$$

where k denotes the number of factors and C_o the number of center replicates. With k=3 and C_o=3, a total of N=15 runs were generated and executed in randomized

order before model fitting. These choices were adopted because BBD efficiently estimates curvature with only three factor levels (−1, 0, +1) and avoids extreme corner combinations, which is advantageous for electroanalytical systems (Table 1). Unlike the traditional one-factor-at-a-time (OFAT) approach, which often misses synergistic or antagonistic interactions between variables, the BBD efficiently reveals these complex interactions while significantly reducing the number of required experimental runs. The center points were used for the determination of error. Based on the experimental data, a second-order polynomial model was obtained, which correlates the relationship between the response and the studied variables. The relationship could be expressed in an equation [54]

$$Ip = b_0 + b_1x + b_2y + b_3z + b_{11}x^2 + b_{22}y^2 + b_{33}z^2 + b_{12}x*y + b_{13}x*z + b_{23}y*z \quad (1)$$

where I_p is the predicted response value (peak current, I_p); x, y, and z are independent variables; b_0 is the intercept term; b_1, b_2 and b_3 are linear coefficients; b_{12}, b_{13} and b_{23} are cross-product coefficients; and b_{11}, b_{22} and b_{33} are quadratic-term coefficients. All the coefficients of the second polynomial model and the response obtained from the experimental design were subjected to multiple nonlinear regression analyses. The empirical relationships between the response (I_p) and the tested variables were obtained using Minitab.

Table 1. Factors and their levels in a full factorial design.

Factor	Level		
	Low (-1)	Medium (0)	High (+1)
E_{acc} (V, x)	0	0.45	0.9
t_{acc} (s, y)	0	30	60
ΔE (V, z)	0.04	0.07	0.10

While the optimization focused primarily on maximizing the anodic current to ensure high sensitivity, the resulting analytical performance was subsequently validated. The low LOD and high reproducibility obtained under these optimized conditions (discussed in the following sections) confirm that the maximization of Ip did not adversely affect the background current, thereby justifying the single-response approach for this specific application

Preparation of real samples

Five swine-urine specimens were collected from three slaughterhouses in Hue City (Central Vietnam), with two specimens taken at each facility when available. Samples were stored at 4°C and analyzed within 24 hours to ensure stability. As the

specimens were collected as waste products from slaughterhouses post-mortem, specific ethical approval for live animal experimentation was not required. For the blank aliquots, 1.0 mL of urine was mixed with 2.0 mL of BRBS buffer solution, diluted with deionized water to a final volume of 10.0 mL, then centrifuged and filtered through a 0.46 μm membrane [55].

For the spiked aliquots, 1.0 mL of urine was fortified with ceftriaxone (20 μM), combined with 2.0 mL of BRBS, brought to 10.0 mL with deionized water, and processed in the same way (centrifugation and membrane filtration). CEF in both blank and spiked test solutions was determined by DP-ASV using the proposed WS_2–RGO/GCE method [55].

Results and discussions

Characterization of WS_2-RGO

In Figure 1, the Raman spectrum of RGO displays the characteristic D (~1350 cm^{-1}) and G (~1580 cm^{-1}) bands, by which the I_D/I_G ratio is commonly used to reflect defect density in sp^2 carbons. In the WS_2–RGO composite trace, these carbon bands are retained while additional low-wavenumber modes assigned to WS_2, E_{2g} (≈350–356 cm^{-1}) and A_{1g} (≈417–420 cm^{-1}) are observed. A modest attenuation and broadening of the G band together with a gently sloping baseline are noted, which are plausibly attributed to interfacial charge-transfer/strain in TMD–graphene heterostructures and to photoluminescence background from semiconducting WS_2 under visible excitation. These assignments and behaviors are consistent with authoritative Raman treatments of graphene-based carbons and with thickness-dependent phonons and resonance effects in WS_2. These results are similar to some recent publications [56–58].

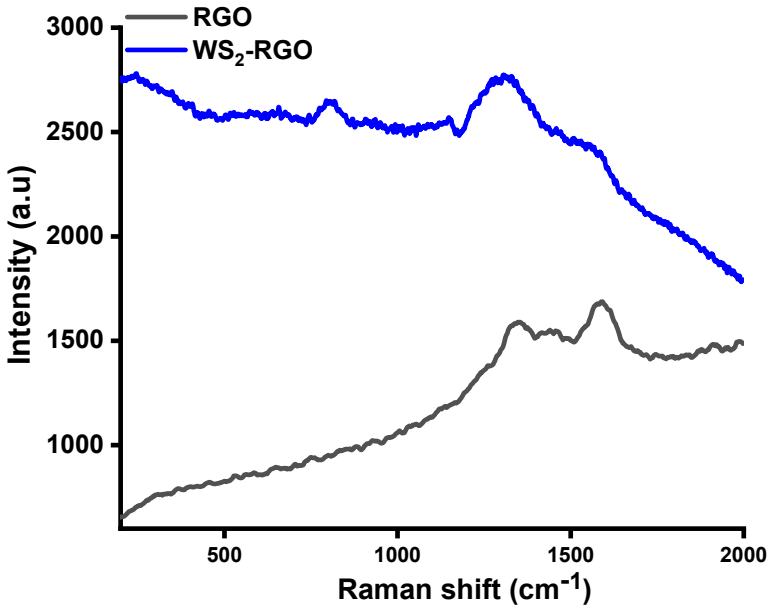

Figure 1. The Raman spectrum of RGO and WS_2-RGO.

View Article Online
DOI: 10.1039/D6SU00059B

In Figure 2a, WS_2 is visualized as plate-like/nanosheet aggregates with locally flower-like assemblies (nanoflowers), a morphology frequently obtained by hydrothermal growth of layered sulfides [59]. In Figure 2b, RGO exhibits the expected wrinkled/crumpled sheet network associated with partial deoxygenation and restacking of graphene oxide [60]. In Figure 2c, WS_2 nanosheets are seen anchored on and interleaved with the conductive RGO scaffold, an arrangement typically associated with increased accessible surface area and shortened charge-transport pathways in 2D heterostructures [61]. Furthermore, this highly open, interleaved morphology effectively prevents graphene sheet restacking, creating expanded diffusion channels that facilitate rapid transport of the bulky ceftriaxone molecules directly to the embedded electroactive sites. These morphologies agree with prior SEM observations of hydrothermal WS_2 nanosheets/nanoflowers and with reviews on wrinkled RGO architectures, similar to several recent reports [59–61]. The textural properties of the composite were further investigated via nitrogen adsorption-desorption measurements, as presented in Figure 2d. The isotherm exhibits a Type IV profile with a distinct H3-type hysteresis loop, which is characteristic of mesoporous structures formed by slit-shaped pores within the aggregated nanosheets. From this isotherm, the specific surface area was calculated to be 135.6 $m^2 g^{-1}$ using the Brunauer–Emmett–Teller (BET) method. This substantial surface area is attributed to the effective prevention of RGO restacking by the intercalated WS_2 nanosheets. Consequently, a higher density of exposed electroactive sites is provided, electrolyte infiltration and enhancing the adsorption capacity for the analyte.

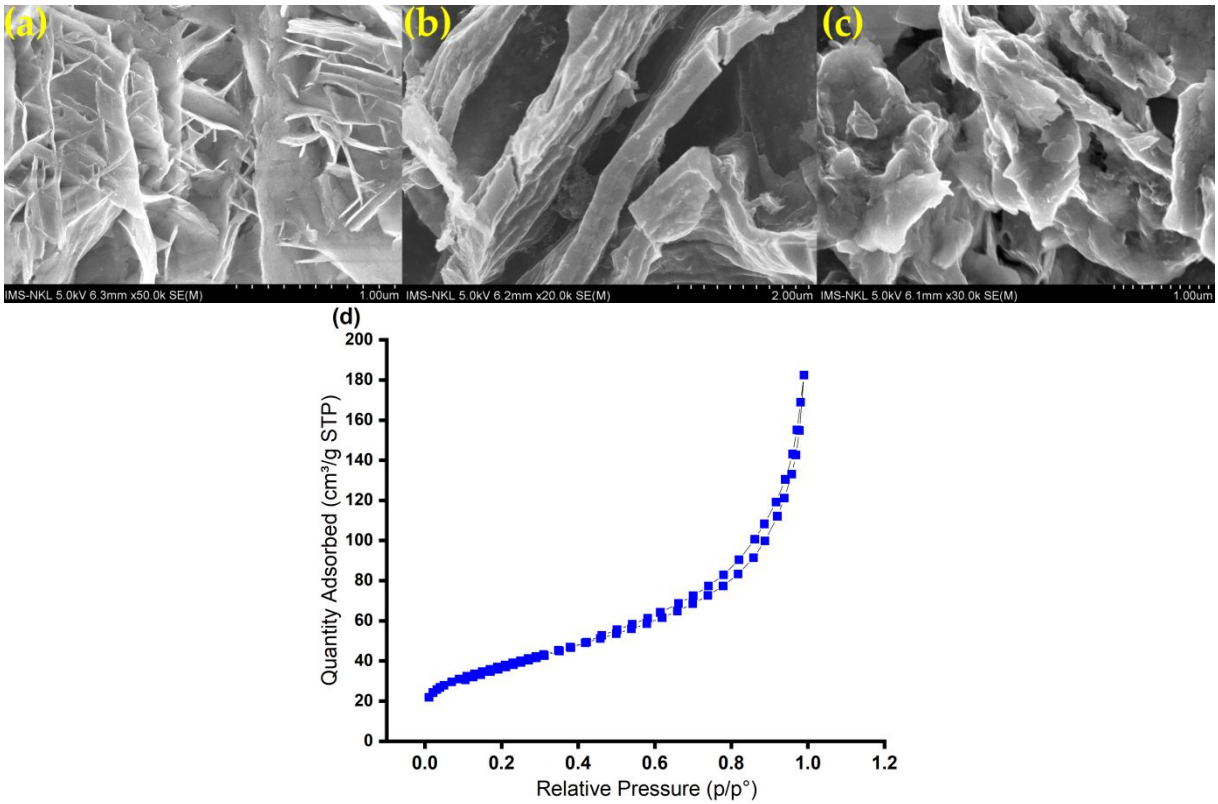

Figure 2. SEM images of (a) WS_2, (b) RGO, (c) WS_2-RGO, (d) Nitrogen adsorption/desorption isotherms of WS_2-RGO.

View Article Online
DOI: 10.1039/D6SU00059B

In Figure 3a, the EDX spectrum reveals signals from C/O (RGO framework) and W/S (WS_2 phase). The elemental maps in Figure 3b–e show co-localization of W and S across the carbon scaffold, indicating that WS_2 is uniformly distributed throughout the RGO network rather than phase-segregated. The use of EDX mapping to confirm homogeneous dispersion of WS_2 on RGO is well established in closely related WS_2/RGO systems and TMD/graphene hybrids [62–64]. The successful formation of the composite is quantitatively validated by the EDX analysis (inset of Figure 3a), which yields atomic percentages of C (80.77%), O (17.52%), W (1.03%), and S (0.68%). This stoichiometry, combined with the uniform elemental mapping in Figure 3b-e and the characteristic vibrational modes observed in Raman spectroscopy, provides robust evidence for the uniform anchoring of WS_2 nanostructures within the RGO network.

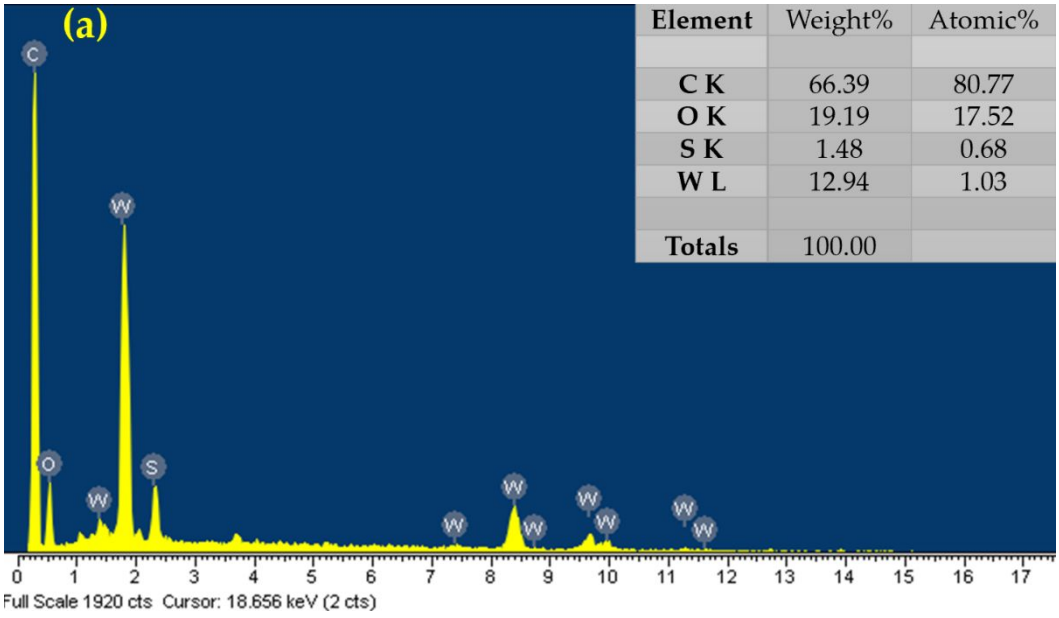

Element	Weight%	Atomic%
C K	66.39	80.77
O K	19.19	17.52
S K	1.48	0.68
W L	12.94	1.03
Totals	100.00	

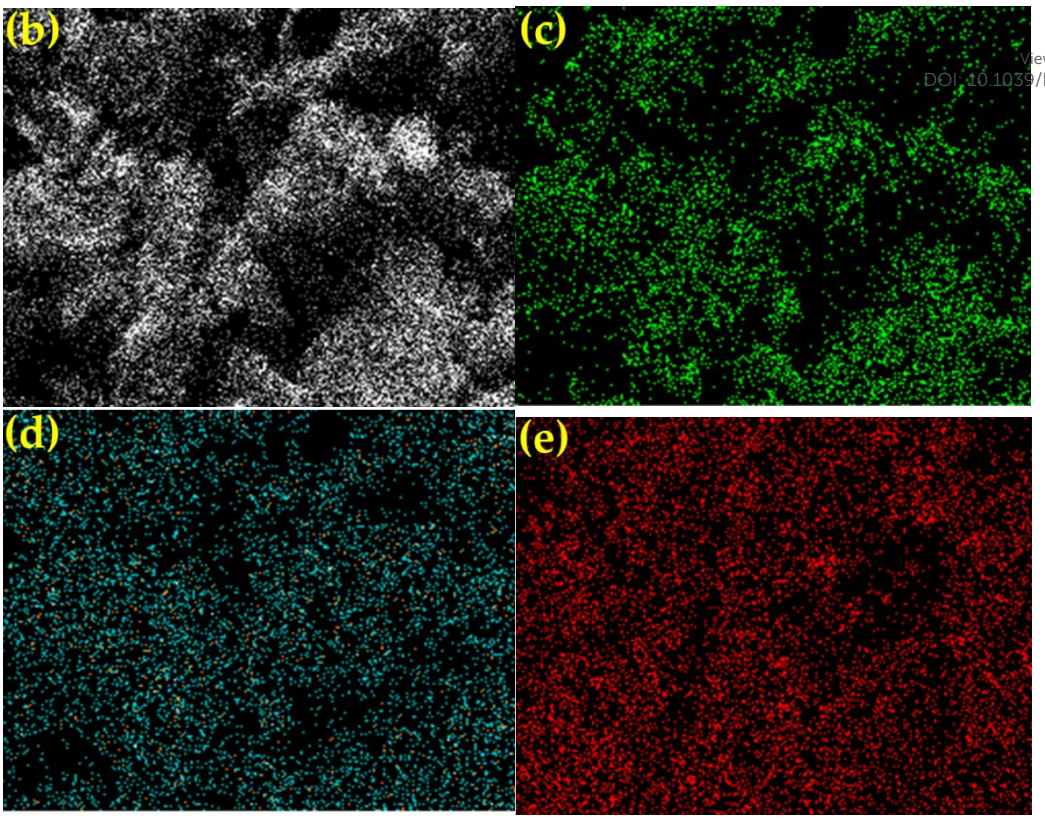

Figure 3. (a) EDX result of WS_2-RGO, (b-e) The element distribution of C, O, S, and W.

The electrochemical detection of ceftriaxone by WS_2-RGO/GCE

Cyclic voltammetry

In Figure 4a, comparative CVs recorded at the bare GCE, RGO/GCE, WS_2/GCE, and WS_2–RGO/GCE in the presence of CEF are displayed, alongside the background scan of the optimized WS_2–RGO/GCE in the absence of the analyte. Notably, the blank scan in the pure buffer solution exhibits a stable capacitive background with no observable faradaic peaks within the investigated potential window. This clearly confirms that the prominent, well-defined anodic peak obtained at roughly 0.96 V is exclusively attributed to the electrochemical oxidation of CEF. Compared to the single-component material-based electrodes and the bare GCE, the WS_2–RGO/GCE delivered a significantly larger and sharper analytical signal [9]. The enhancement has been attributed to the synergistic interface, which maximizes the effective electroactive surface area and conductivity, thereby facilitating heterogeneous electron transfer and leading to substantial signal amplification without a significant shift in oxidation potential. Specifically, within this synergistic framework, the highly conductive RGO network serves as a rapid 'electron highway' that minimizes charge-transfer resistance, while the uniformly anchored WS_2 nanosheets provide abundant edge-rich catalytic sites for the oxidation reaction. Therefore, WS_2-RGO/GCE has been selected for the next measurements.

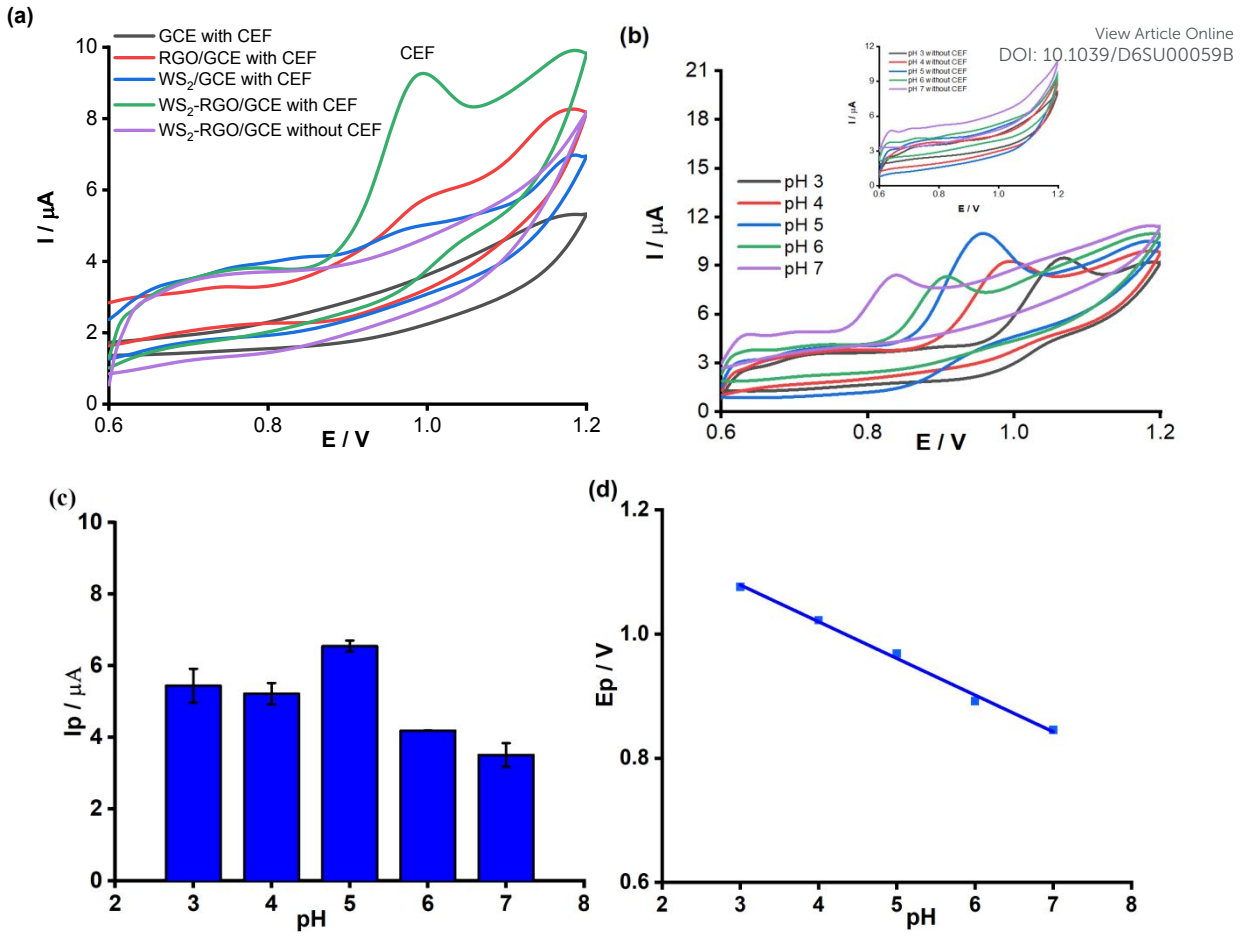

Figure 4. (a) The CVs of CEF at several electrodes, (b) CVs of CEF with various pH values using WS_2-RGO/GCE (inset: CVs for WS_2-RGO/GCE at different pH in the absence of CEF), (c) Plot of *Ip vs.* pH, and (d) The linear plot of *Ep versus* pH.

Experimental conditions: 5 µM CEF in the solution, including BRBS 0.2 M, scan rate: 0.2 V/s, potential range from +0.6 V and +1.2 V.

Figure 4b presents CVs collected in BRBS at pH 3–7 using the selected WS_2-RGO/GCE. A progressive shift of the oxidation peak toward less positive potentials was observed with increasing pH, indicating the involvement of protons in the rate-determining step of CEF oxidation. Peak shape and baseline stability were preserved across the series, suggesting that the supporting electrolyte afforded suitable buffering without introducing significant capacitive distortion. To rigorously verify the baseline stability and ensure that the observed shifts originated solely from the analyte, cyclic voltammograms of the WS_2–RGO/GCE were recorded in the absence of ceftriaxone across the pH range of 3.0 to 7.0 (Figure 4b, inset). No significant redox peaks were detected in the blank buffer solutions, and a low, stable capacitive background current was maintained independent of the pH variation. This confirms that the supporting electrolyte does not contribute interfering signals within the working potential window, thereby allowing for the accurate normalization of the analytical current and

validating the attribution of the anodic peaks in the main panel exclusively to the oxidation of CEF.

View Article Online
DOI: 10.1039/D6SU00059B

Figure 4c summarizes the dependence of the anodic peak current (*Ip*) on pH. An increase in *Ip* from pH 3 to a maximum at pH 5 was recorded, followed by a gradual decrease toward near-neutral conditions. This profile is consistent with proton-coupled electron transfer at a WS_2-RGO/GCE interface: excessive protonation in strongly acidic media can depress apparent kinetics, whereas diminished proton activity at higher pH reduces the overall rate of the coupled step. At pH 5, a balance between interfacial proton availability and charge-transfer efficiency appears to be achieved, yielding the highest analytical signal under otherwise identical conditions. Therefore, pH 5 is picked for further experiments, similar to the recent publication [48]. At the optimized pH of 5.0, the anodic peak potential (Epa) at the WS_2–RGO/GCE was observed at +0.96 V. Considering the pKa values of ceftriaxone (pKa1 ≈ 3.0 and pKa ≈ 4.0), the drug molecule exists predominantly in an anionic state at pH 5.0. This specific protonation state optimally balances the availability of protons required for the electrochemical reaction while allowing favorable non-covalent interactions (such as π-π stacking) with the WS_2-RGO surface, ultimately driving the highest oxidation current.

While electrostatic repulsion between the anionic binder and the deprotonated analyte at pH 5 presents a potential barrier, the experimental results demonstrate that this effect is negligible. The adsorption process is driven primarily by strong π-π stacking interactions between the ceftriaxone molecule and the WS_2–RGO scaffold, which effectively overcome the electrostatic resistance from the dilute binder, ensuring unimpeded electron transfer kinetics. Figure 4d shows a linear decrease of the peak potential (*Ep*) with pH over the range 3–7. The slope lies in the expected magnitude for proton-involved oxidations, supporting a proton-coupled mechanism and indicating that the driving force varies predictably with medium acidity—an attribute favorable for method robustness and transferability.

$$Ep = (-0.059 \pm 0.002)\text{pH} + (1.257 \pm 0.013) \qquad R^2 = 0.995$$

With the assistance of the Nernst equation, at 298K (25 °C), the relationship of E_p and pH of a pair of redox and conjugate could be illustrated as follows:

$$E_p = E^0 + \frac{0.059}{n} log \frac{\text{Ox}}{R} - 0.059 \frac{n}{p} pH$$

The slope value of the E_p versus pH graph is −0.059, which is near the Nernstian value of −0.059 (Figure 4d). This value corresponds to n/p equal to 1, illustrating that the CEF oxidation within the modified electrode contains equal electrons and protons. As depicted in Scheme 1, the electrochemical oxidation specifically occurs at the

View Article Online
DOI: 10.1039/D6SU00059B

aminothiazole group of the ceftriaxone molecule, undergoing a distinct two-electron and two-proton transfer process, which is consistent with the recent report [48,65]:

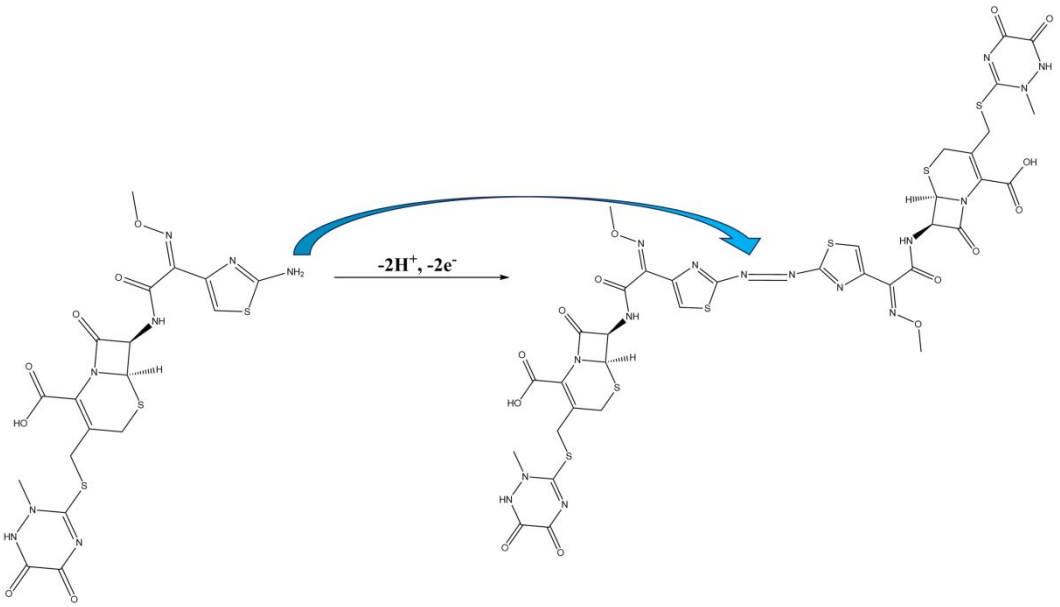

Scheme 1. The supposed oxidation mechanism of the aminothiazole group of CEF [48].

Response surface methodology (RSM) and Box-Behnken design (BBD)

A compact Box–Behnken campaign was executed to interrogate the three-factor space (E_{acc}, t_{acc}, ΔE), with the randomized run matrix and measured peak currents compiled in Table 2. The inclusion of three center-point replicates provided pure-error estimates for lack-of-fit testing, and the response span (≈1.19–1.85 μA) indicated adequate excitation of curvature without resorting to extreme settings. Model-quality statistics reported alongside Table 2 (S = 0.0274; PRESS = 0.0350; R^2 = 99.23%; R^2_{adj} = 92.88%; R^2_{pred} = 97.86%) further supported a precise quadratic description over the design domain [66].

Table 2. Box–Behnken design matrix generated in Minitab (coded factors x, y, z) and measured CEF peak current responses, $I_{p,\,CEF}$ (μA).

No.	Factors			$I_{p,\,CEF}$ (μA)
	x	y	z	
1	0	0	0	1.73036
2	-1	0	-1	1.38503
3	1	-1	0	1.19348
4	-1	1	0	1.48038
5	1	0	-1	1.27471

6	0	-1	-1	1.31807
7	0	0	0	1.67183
8	1	0	1	1.56462
9	0	0	0	1.68758
10	0	1	-1	1.51066
11	0	1	1	1.84701
12	-1	0	1	1.62245
13	1	1	0	1.42249
14	-1	-1	0	1.33941
15	0	-1	1	1.61478
S	**PRESS**	**R-sq**	**R-sq(adj)**	**R-sq(pred)**
0.0274	0.0350	99.23%	92.88%	97.86%

Based on the experimental data (Table 3), three equations of the experimental design were established using Minitab. They correlate the relationship between the peak current of CEF and the three variables.

$$Ip = 0.9857 + 0.777x + 0.00936y + 5.72z$$
$$-1.1076x*x - 0.0001260y*y - 11.8z*z + 0.00163x*y + 0.97x*z + 0.0110y*z$$

Table 3. Regression coefficients and significance for the quadratic BBD of $I_{p,\,CEF}$.

Term	Coef	SE Coef	T-Value	P-Value	VIF
Constant	1.6966	0.0158	107.06	0.000	
x	-0.04650	0.00970	-4.79	0.005	1.00
y	0.09935	0.00970	10.24	0.000	1.00
z	0.14505	0.00970	14.95	0.000	1.00
x^2	-0.2243	0.0143	-15.70	0.000	1.01
y^2	-0.1134	0.0143	-7.94	0.001	1.01
z^2	-0.0106	0.0143	-0.74	0.491	1.01
x*y	0.0220	0.0137	1.60	0.170	1.00
x*z	0.0131	0.0137	0.96	0.383	1.00
y*z	0.0099	0.0137	0.72	0.503	1.00

Table 4. Analysis of Variance (ANOVA) for the quadratic regression model.

Source	DF	Adj SS	Adj MS	F-Value	P-Value
Model	9	0.488325	0.054258	72.02	0.000

Linear	3	0.264572	0.088191	117.06	0.000
x	1	0.017295	0.017295	22.96	0.005
y	1	0.078963	0.078963	104.81	0.000
z	1	0.168313	0.168313	223.41	0.000
Square	3	0.220734	0.073578	97.66	0.000
x^2	1	0.185743	0.185743	246.54	0.000
y^2	1	0.047449	0.047449	62.98	0.001
z^2	1	0.000415	0.000415	0.55	0.491
2-Way Interaction	3	0.003019	0.001006	1.34	0.362
x*y	1	0.001938	0.001938	2.57	0.170
x*z	1	0.000689	0.000689	0.91	0.383
y*z	1	0.000393	0.000393	0.52	0.503
Error	5	0.003767	0.000753		
Lack-of-Fit	3	0.001932	0.000644	0.70	0.633
Pure Error	2	0.001835	0.000917		
Total	14	0.492092			

The ANOVA in Table 4 demonstrated that the quadratic model was highly significant (F = 72.02, $p < 0.001$), with both the linear block (F = 117.06) and the square block (F = 97.66) contributing strongly. Among single-factor effects, ΔE (z) emerged as the dominant positive contributor (F = 223.41), followed by t_{acc} (y; F = 104.81), whereas E_{acc} (x) exerted a smaller, negative effect (F = 22.96). Pronounced downward curvature in x^2 (F = 246.54) and y^2 (F = 62.98) contrasted with a non-significant z^2 term ($p = 0.491$), and all two-factor interactions were negligible; the lack-of-fit test was not significant (p = 0.633). Taken together, these results describe a well-behaved surface dominated by main effects, with an interior optimum shaped primarily by curvature in E_{acc} and t_{acc}, and an approximately linear benefit from increasing ΔE within the tested range, an outcome that is consistent with the interfacial-mechanics rationale developed in the Introduction and with the response-surface visualizations that follow.

The linear effects were ordered as $|\beta_z| > |\beta_y| > |\beta_x|$, with z and y contributing positively and x negatively to Ip. Significant negative quadratic terms indicated downward curvature in x and y, whereas the z^2 term was statistically insignificant over the explored range. All pairwise interactions were estimated to be small and statistically insignificant, and the lack-of-fit test was not significant. Importantly, the statistical insignificance of these two-factor interaction terms indicates the method's robustness; it implies that the main operational factors act independently, thereby simplifying practical control and routine execution of the analytical procedure.

Collectively, these results support a well-behaved surface dominated by main effects, with an interior optimum primarily governed by curvature in both *x* and *y*.

Excellent model adequacy was further suggested by the statistics (S = 0.0274; PRESS = 0.0350; R^2 = 99.23%; R^2_{adj} = 92.88%; R^2_{pred} = 97.86%), consistent with a stable quadratic description within the Box–Behnken domain.

These coefficient signs and magnitudes rationalize the response-surface graphics. In Figure 5, the x–y, x–z, and y–z plots display a single smooth maximum, with pronounced curvature along x and y and a comparatively near-planar behavior along z, aligning with the significant x^2/y^2 and insignificant z^2 terms, respectively. The weak interaction estimates explain the largely additive appearance of the surfaces.

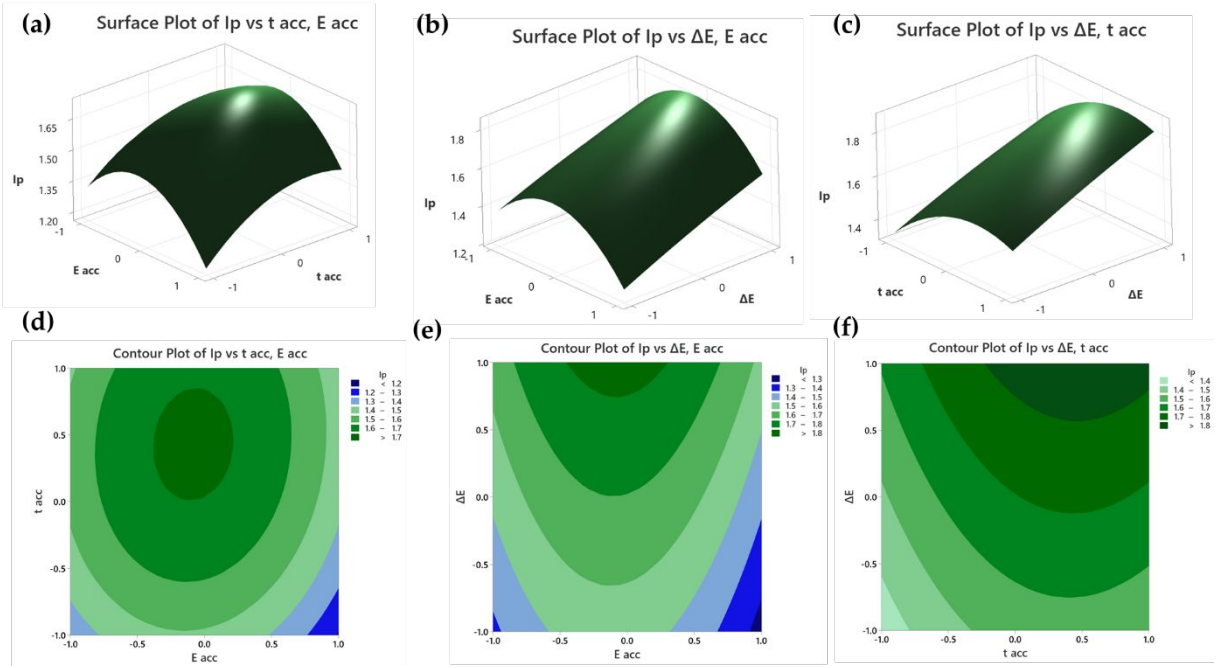

Figure 5. Contour and response surface plots of the peak current (*Ip*) as a function of the interaction between factors: (a,d) accumulation potential (E_{acc}) and accumulation time (t_{acc}); (b,e) accumulation potential (E_{acc}) and pulse amplitude (ΔE); (c,f) accumulation time (t_{acc}) and pulse amplitude (ΔE)..

Model-based optimization yielded a unique interior setting. Under these conditions, replicate voltammograms (Figure 6) evidenced stable signals, and the experimental mean current agreed closely with the model prediction (Table 5): I_p^{exp}=1.8381±0.1355 μA (n = 5) versus I_p^{pred}=1.8579 μA; a one-sample t-test gave p = 0.735>0.05, indicating no statistically significant difference between predicted and observed values and thereby validating the optimization.

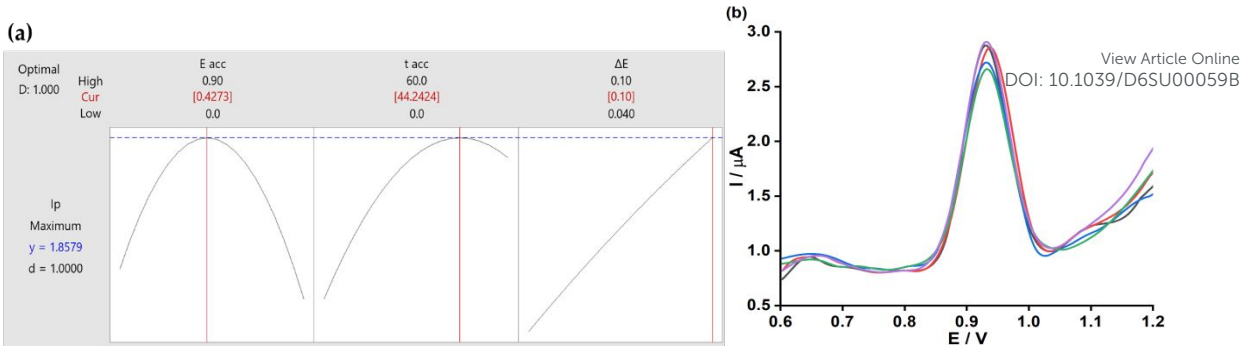

Figure 6. (a) Optimization plot for peak current of CEF oxidation, (b) DP-ASV curves obtained at the WS_2-RGO/GCE prepared at optimization conditions (C_{CEF} = 1 μM in a 0.2 M BRBS buffer solution, pH 5).

Table 5. $I_{p,\,CEF}$ at the optimized conditions with n=5.

I_p^{exp} (μA)	I_p^{pred} (μA)	p in One-sample T-test
1.8381 ± 0.1355(*)	1.8579	0.735

(*)*Mean ± SD (n=5)*

Taken together, the regression equation captures the dominant, monotonic benefits of increasing t_{acc} and ΔE within the tested bounds, the performance penalty associated with over-polarization at extreme E_{acc} or excessive t_{acc}, and the absence of meaningful two-factor synergy. The figures and confirmation data establish a coherent narrative from modeling (equation) to visualization (Figure 5), prediction and operationalization (Figure 6), and statistical verification (Table 5), providing a sound basis for subsequent analytical evaluations under the optimized conditions.

Differential pulse voltammetry

The DP-ASV curves of CEF with several concentrations in a 0.2 M BRBS buffer solution (pH = 5) are illustrated in Figure 7a. Figure 7b describes the linear concentration that ranged from 0.02 to 12.08 μM, including the linear regression equation as follows:

$$Ip\ (\mu A) = (1.72 \pm 0.05)C_{CEF,\,\mu M} + (0.28 \pm 0.02)\quad R^2 = 0.996$$

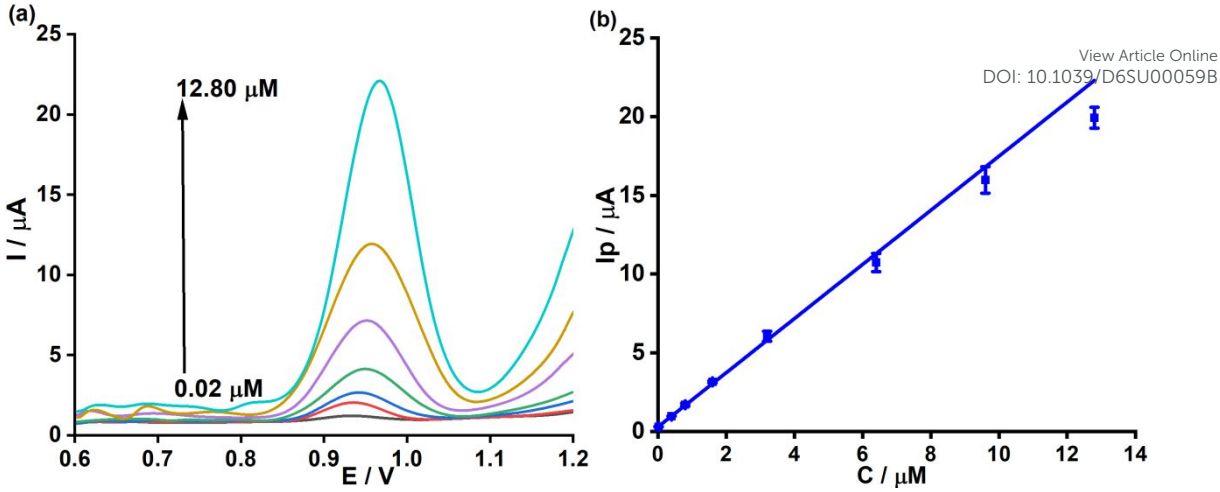

Figure 7. (a) DP-ASV of CEF at 0.02, 0.4, 0.8, 1.6, 3.2, 6.40, 9.60, and 12.80 µM employing WS_2-RGO/GCE and (b) The relationship between *Ip* and $C_{CEF,\ \mu M}$. *Experimental conditions: Potential range from +0.6 V to +1.2 V in the buffer solution BRBS 0.2 M (pH 5.0).*

The LOD for CEF, calculated by the 3σ criterion, was 0.009 µM. As summarized in Table 1, the linear working range and LOD obtained with the WS_2-RGO/GCE are compared with values reported for related modified electrodes. From Table 6, the present sensor offers a wide linear range and a low LOD, with performance broadly comparable to previously reported systems. Beyond comparable sensitivity, the distinct advantage of the proposed WS_2-RGO sensor lies in its sustainability; the facile hydrothermal synthesis provides a far greener, simpler fabrication route compared to the complex, multi-step procedures typically reported. On this basis, the WS_2–RGO/GCE is considered suitable for laboratory determination of ceftriaxone in real samples.

Table 6. Reported analytical figures of merit for electrochemical determination of ceftriaxone using various modified electrodes, with the present WS_2–RGO/GCE included for comparison

No.	Electrode	Method	Range linear (µM)	LOD (µM)	Ref.
1	CuHCF/PGE	AMP	2 - 72	0.54	[67]

2	CAC-PU/PtE	DP-ASV	100 – 1500	52	8
3	PtNPs/MWCNT/GCE	DP-ASV	0.01-10	0.009	10
3	RGO/MIP/PDPA/GCE	DP-ASV	0.03 – 3.08	0.008	68
4	CNT/GCE	DP-ASV	20 - 1000	4.03	9
5	HMDE	DP-ASV	99 – 810	29	69
6	$NiFe_2O_4$-NPs/GCE	DP-ASV	0.01 – 3.2	0.002	7
7	SPE/SiO_2/ZrO_2/N-doped CDs	SWV	0.008 – 40	0.0002	48
8	WS_2-RGO/GCE	DP-ASV	0.02 – 12.8	0.009	This work

Note: CuHCF/PGE: Copper hexacyanoferrate/pencil graphite electrode, CAC-PU/PtE: caffeic acid and chitosan-polyurethane films modified platinum electrode, PtNPs/MWCNT: Platinum nanoparticle decorated multiwalled carbon nanotube, RGO/MIP/PDPA: Reduced graphene oxide/molecular imprinted polymer/poly-diphenylamine, CNT: carbon nanotube, HMDE: Hanging mercury drop electrode, SPE/SiO_2/ZrO_2/N-doped CDs: screen-printed electrode/silicon oxide/zirconium oxide/nitrogen-doped carbon quantum dots, AMP: amperometry, DP-ASV: differential pulse voltammetry.

Interferents

The influence of common organic and inorganic constituents on the DPV voltammetric response of CEF was assessed by introducing each species at large excess with respect to the analyte (interferent-to-CEF molar ratios of 80–190) (Table 7). The relative error in peak current (*RE*, %) remained within ±5% for all tested species, which is generally regarded as an acceptable variation for electroanalytical measurements performed in complex matrices.

Organic electroactive compounds produced small positive deviations: hypoxanthine (100-fold) yielded RE = +4.5%, clenbuterol (100-fold) +3.9%, ascorbic acid

(150-fold) +4.9%, and uric acid (190-fold) +2.7%. These results indicate that possible co-oxidation or background contributions from these species were limited under the selected conditions. The modest increase observed with ascorbic acid, despite a 150-fold excess, suggests that capacitive currents or overlapping faradaic processes were effectively mitigated by the chosen waveform and the interfacial properties of the modified electrode.

Inorganic salts caused very small negative or positive shifts: $(NH_4)_2SO_4$ (100-fold) gave RE = −4.4%, NaCl (150-fold) −0.6%, $Ca(NO_3)_2$ (150-fold) −4.3%, and $FeCl_3$ (80-fold) +3.1%. The slight decreases in sulfate- and nitrate-containing salts can reasonably be attributed to ionic-strength effects and double-layer compression, which reduce the effective interfacial concentration of the analyte. The small positive deviation observed in the presence of Fe^{3+} (+3.1%) remains well within the defined tolerance limit (< ±5%). This confirms that the sensor maintains adequate selectivity even in the presence of common ionic species found in physiological fluids.

Taken together, the data demonstrate that the analytical signal for CEF is tolerant to large excesses of typical coexisting species at pH 7. Under these conditions, no individual interferent exceeded |RE| = 5%, and the most demanding cases, ascorbic acid (+4.9%) and $(NH_4)_2SO_4$ (−4.4%), still met the acceptance criterion. The results support the practical applicability of the nanomaterial-modified GCE for determinations of CEF in samples where these compounds are likely to be present, without requiring extensive sample cleanup. Furthermore, it should be emphasized that this excellent selectivity is strongly bolstered by the specific DPV waveform; the optimized pulse parameters efficiently discriminate the target faradaic signal from overlapping background and capacitive currents.

Table 7. The influence of interferences on the peak current of CEF (5 μM CEF in 0.2 M BRBS buffer solution, pH 7)

Interference	$C_{interference}$: C_{CEF}	*RE* (%)
hypoxanthine	100	4.5
clenbuterol	100	3.9
Ascorbic acid	150	4.9
Uric acid	190	2.7
$(NH_4)_2SO_4$	100	-4.4
NaCl	150	-0.6
$FeCl_3$	80	3.1
$Ca(NO_3)_2$	150	-4.3

Repeatability, reproducibility and long-term stability

View Article Online
DOI: 10.1039/D6SU00059B

Repeatability is a basic requirement for electrochemical electrodes, underpinning their suitability for *in situ* use (Figure 8). Repeatability was evaluated by recording seven successive DP-ASV measurements with a single WS_2-RGO/GCE at four CEF levels: 0.02 μM (Figure 8a), 0.4 μM (Figure 8b), 3.2 μM (Figure 8c), and 12.8 μM (Figure 8d). Peak positions and shapes remained essentially unchanged, giving RSDs of 3.3%, 1.4%, 1.6% and 1.2%, respectively. These RSDs are well below ½.$RSD_{Horwitz}$ ($RSD_{Horwitz}$= $2^{1-0.5\log C}$, in that *C*, is the fraction concentration of the analysis compound), which would be 22.6%, 16.9%, 12% and 9% at the corresponding concentrations [70]. The results, therefore, indicate good repeatability for the WS_2-RGO/GCE across the tested range and support its repeated use for CEF determinations [71].

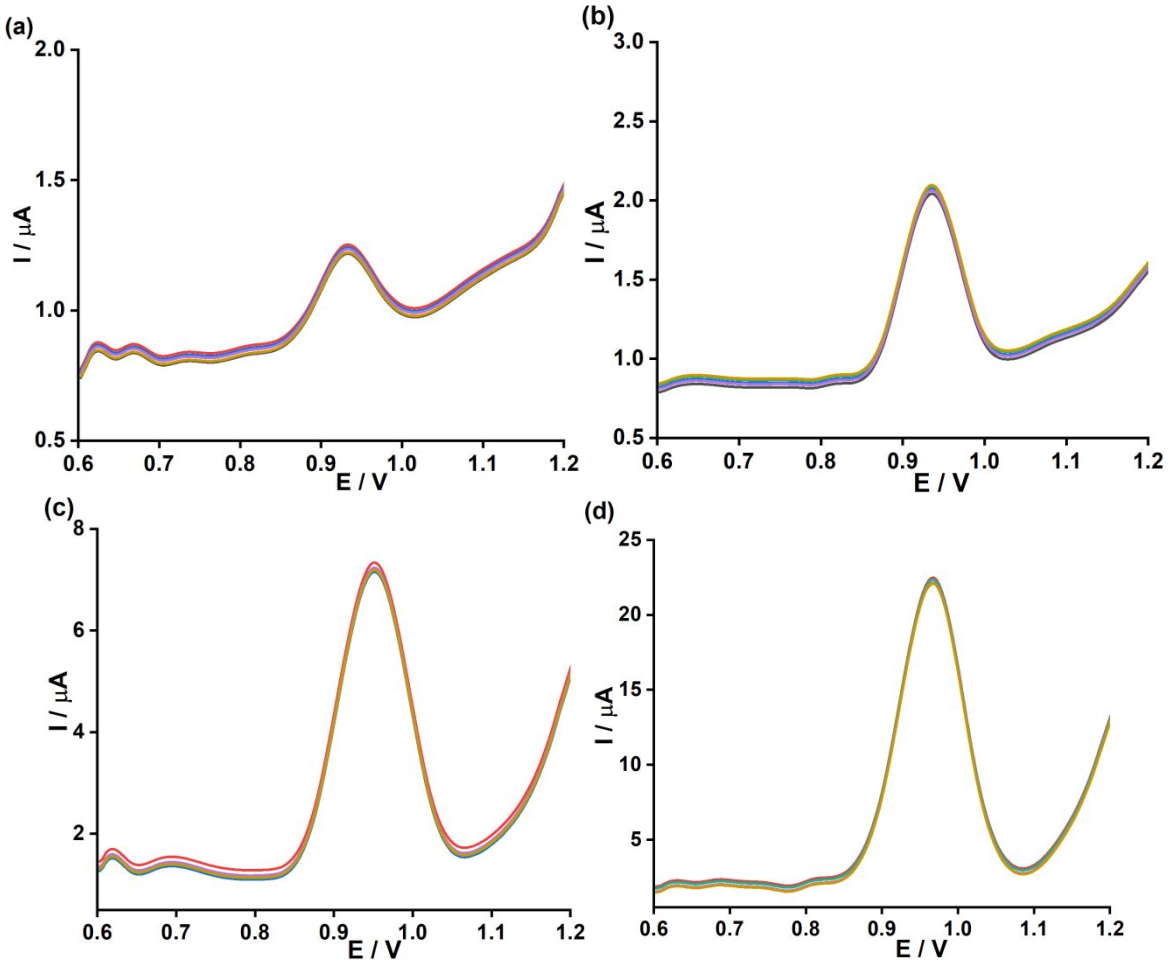

Figure 8. DP-ASV of CEF with 7 times repeated measurements at (a) 0.02 μM, (b) 0.4 μM, (c) 3.2 μM, and (d) 12.8 μM on WS_2-RGO/GCE.

View Article Online
DOI: 10.1039/D6SU00059B

Reproducibility was assessed at a CEF level of 0.02 μM in 0.2 M BRBS buffer (pH = 5) (Figure 9). DP-ASV were recorded using five independently fabricated WS_2–RGO/GCEs (i.e., five separate modifications on fresh bare GCEs). Highly consistent signals were obtained, yielding an RSD of 3.8%. These results demonstrate satisfactory between-electrode reproducibility and, together with the repeatability data, support the reliability of the WS_2–RGO/GCE for ceftriaxone determination.

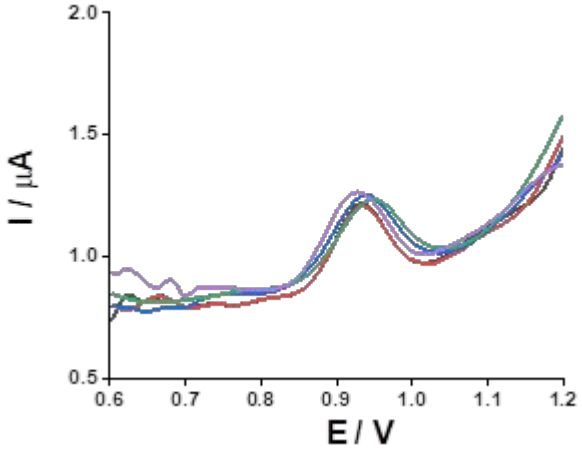

Figure 9. DP-ASV of CEF with 5 times of modification onto a GCE by WS_2-RGO at 0.02 μM with the same procedure.

Real samples

Urine samples were analyzed by DP-ASV at the WS_2–RGO/GCE and by HPLC as a reference. As summarized in Table 8, the unspiked aliquots contained no detectable CEF by either method. After fortification at 20 μM, the DP-ASV procedure furnished recoveries in the 96.8–103.8% range, while HPLC determinations on the same aliquots yielded concentrations close to the spiked level (19.22–20.81 μM). It should be noted that the LOD was determined under optimized buffer conditions. However, analysis of blank urine samples confirmed the absence of interfering peaks, and the quantitative recovery of spiked samples at clinically relevant concentrations demonstrates the method's effective sensitivity in the biological matrix. This straightforward 10-fold dilution step was crucial, as it effectively minimized the severe 'matrix effects' caused by the complex macromolecular composition of raw urine, thereby ensuring the high recovery rates and accuracy observed during the analysis.

A paired-sample *t*-test was applied to compare DP-ASV and HPLC across the five matrices. The statistic $t(4) = 0.589$, $p = 0.587 > 0.05$, indicated no statistically significant difference at $\alpha = 0.05$. These outcomes show that, under laboratory conditions, the proposed WS_2–RGO electrochemical method provides accurate, matrix-tolerant quantification of ceftriaxone and performs comparably to HPLC, supporting its use for subsequent validation studies in real applications.

Table 8. Analysis comparison of ceftriaxone in actual urine samples using DP-ASV (WS_2–RGO/GCE) and HPLC methods

Sample	CEF added (μM)	DP-ASV		HPLC
		Founded (μM)	Rev(%)	Founded (μM)
Urine #1	0	0	101.5	0
	20	20.30 ± 0.03(*)		19.22 ± 0.01
Urine #2	0	0	96.8	0
	20	19.36 ± 0.01		20.74 ± 0.07
Urine #3	0	0	101.2	0
	20	21.25 ± 0.06		20.81 ± 0.04
Urine #4	0	0	103.8	0
	20	20.77 ± 0.10		19.70 ± 0.02
Urine #5	0	0	99.7	0
	20	19.94 ± 0.05		19.82 ± 0.01

* *mean ± standard deviation (n = 3)*

Conclusions

In this study, a sensitive electrochemical platform based on a WS_2–RGO heterostructure was successfully developed for the determination of ceftriaxone. The experimental characterization confirmed the formation of a uniform composite where WS_2 nanosheets are distributed on the conductive RGO network, effectively preventing restacking and enhancing the accessible electroactive surface area. The electrochemical performance, optimized via response surface methodology, demonstrated superior electron transfer kinetics and significantly higher sensitivity compared to single-component or unmodified electrodes. The method yielded a low limit of detection (0.009 μM) and excellent precision, with applicability validated through high recovery rates in complex swine urine matrices. These findings confirm that the WS_2–RGO interface provides a stable and robust transduction layer for electroanalysis. Consequently, the proposed sensor offers a practical, cost-effective alternative for the routine screening of antibiotic residues, directly addressing the urgent need for monitoring ceftriaxone in the context of food safety and *Streptococcus suis* risk management.

Author contributions

Mofassel Hossen Akash conceptualized, designed the experiment, performed data analysis, and contributed to the draft and final manuscript writing. Shukanta

View Article Online
DOI: 10.1039/D6SU00059B

Bhowmik reviewed the draft version and assisted in preparing the final manuscript. Md. Abdus Samad Azad and Nahid Sultana assisted in drafting the manuscript. Md. Ashraful Alam supervised the entire project and coordinated and managed the necessary facilities.

Conflicts of interest

The authors declare that they have no conflicts of interest.

Data availability

The data that support the findings of this study are available from the corresponding author upon request.

Reference

1 O. Cohen and D. Denning, *Clin. Infect. Dis.*, 2017, cix059.

2 W. H. Organization, *The WHO AWaRe (access, watch, reserve) antibiotic book*, World Health Organization, 2022.

3 L. Q. Huong, T. T. T. Hang, P. T. Ngoc, C. Van Tuat, V. I. Erickson and P. Padungtod, *J. Food Prot.*, 2020, **83**, 1701–1706.

4 K. N. Woodward, *Vet. Pharmacovigil. Advers. React. to Vet. Med. Prod.*, 2009, 547–567.

5 H. E. Brindle, M. Choisy, R. Christley, N. French, M. Griffiths, P. Q. Thai, H. R. van Doorn and B. Nadjm, *Front. Public Heal.*, 2025, **12**, 1396915.

6 Q. Wang, M. Wang, N. Zhang, X. Huang, X. Wang and S. Wang, *Microchem. J.*, 2023, **189**, 1–29.

7 K. Akhtar, J. A. Baig, S. A. Solangi, S. Hussain, H. E. Ali, S. Perveen, T. G. Kazi and H. I. Afridi, *Microchem. J.*, 2023, **191**, 108808.

8 C. Ben Ali Hassine, Ö. Güngör, M. Burç, İ. Özcan, S. Köytepe and S. Titretir Duran, *Polym. Technol. Mater.*, 2022, **61**, 609–623.

9 S. Majdi, A. Jabbari, H. Heli, H. Yadegari, A. A. Moosavi-Movahedi and S. Haghgoo, *J. Solid State Electrochem.*, 2009, **13**, 407–416.

10 S. Shahrokhian, N. Hosseini-Nassab and Z. Kamalzadeh, *J. Solid State Electrochem.*, 2014, **18**, 77–88.

11 T. Ndlovu, O. A. Arotiba, S. Sampath, R. W. Krause and B. B. Mamba, *Sensors*, 2012, **12**, 11601–11611.

12 M. A. Alvarez, M. Ruidíaz-Martínez, G. Cruz-Quesada, M. V. López-Ramón, J. Rivera-Utrilla, M. Sanchez-Polo and A. J. Mota, *Chem. Eng. J.*, 2020, **379**, 122334.

13 P. A. Kocheril, K. D. Lenz and H. Mukundan, *ECS Sensors Plus*, 2022, **1**, 21601.

14 X. Liang, X. Liu and L. Yao, *ECS Sensors Plus*.

15 V. Chaudhary, A. K. Kaushik, H. Furukawa and A. Khosla, *ECS Sensors Plus*.

16 T. Hyodo, W. Sakata, T. Ueda and Y. Shimizu, *ECS Sensors Plus*, 2022, **1**, 13602.

17 H. L. Atchison, D. A. Wetz, Z. Bailey, M. Davis and J. M. Heinzel, *ECS Sensors Plus*.

18 T. Ueda, N. Oide, K. Kamada, T. Hyodo and Y. Shimizu, *ECS Sensors Plus*, 2022, **1**, 13604.

19 R. Sharma, G. Lakshmi, A. Kumar and P. Solanki, *ECS Sensors Plus*, 2022, **1**, 10603.

20 F. D. S. Santos, L. V. da Silva, P. V. S. Campos, C. de Medeiros Strunkis, C. M. G. Ribeiro and M. O. Salles, *ECS Sensors Plus*, 2022, **1**, 13603.

21 T. Q. Casuse, A. Benavidez, J. B. Plumley, L. Tsui, A.-M. Ali, J. M. Cerrato and F. H. Garzon, *ECS Sensors Plus*, 2022, **1**, 14602.

22 S. Singh, J. Wang and S. Cinti, *ECS Sensors Plus*, 2022, **1**, 023401.

23 R.-I. Stefan-van Staden, *ECS Sensors Plus*, 2022, **1**, 11603.

24 A. Khosla, *ECS Sensors Plus*, 2022, **1**, 10001.

25 R. Fan, Y. Li, K.-W. Park, J. Du, L. H. Chang, E. R. Strieter and T. L. Andrew, *ECS Sensors Plus*.

26 J. Chung, L. Sepunaru and K. W. Plaxco, *ECS Sensors Plus*, 2022, **1**, 11604.

27 A. K. Baytak, S. Duzmen, T. Teker and M. Aslanoglu, *Sensors Actuators B Chem.*, 2017, **239**, 330–337.

28 H. Yin, Y. Zhou, Q. Ma, S. Ai, P. Ju, L. Zhu and L. Lu, *Process Biochem.*, 2010, **45**, 1707–1712.

29 H. Zhang, M. Zhao and Y. Yang, *Biomed. Nanomater.*, 2016, 283–326.

30 A. Nezhadali and M. Mojarrab, *J. Electroanal. Chem.*, 2015, **744**, 85–94.

31 M. J. Allen, V. C. Tung and R. B. Kaner, *Chem. Rev.*, 2010, **110**, 132–145.

32 M. Pumera, *Chem. Soc. Rev.*, 2010, **39**, 4146–4157.

33 Y. Li, T. Wen, C. Xue, Q. Han, Y. Wang, J. Hong, X. Zhou and H. Jiang, *Biosens. Bioelectron.*, 2013, **42**, 287–292.

34 J. V. Piovesan, E. R. Santana and A. Spinelli, *J. Electroanal. Chem.*, 2018, **813**, 163–170.

35 B. C. Lourenção, R. A. Medeiros, R. C. Rocha-Filho, L. H. Mazo and O. Fatibello-Filho, *Talanta*, 2009, **78**, 748–752.

36 L. Chen, Y. Tang, K. Wang, C. Liu and S. Luo, *Electrochem. commun.*, 2011, **13**,

133–137.

View Article Online
DOI: 10.1039/D6SU00059B

37 V. Menaka and D. Geetha, *Ionics (Kiel).*, 2025, 1–17.

38 N. S. Md Rudin, M. A. I. Mohd Yassin and M. F. Omar, *Fullerenes, Nanotub. Carbon Nanostructures*, 2025, 1–9.

39 H. Luo, X. Zhou, X. Guo, Z. Fang, Q. Chen and J. Zhou, *Chemosphere*, 2021, **262**, 128067.

40 E. Moradpur-Tari, R. Sarraf-Mamoory and A. Yourdkhani, *Ceram. Int.*, 2022, **48**, 8563–8571.

41 S. B. Malik, F. E. Annanouch, C. Bittencourt and E. Llobet, *ACS Appl. Mater. Interfaces*, 2025, **17**, 31592–31603.

42 U. T. Uthappa, M. Nehra, R. Kumar, N. Dilbaghi, G. Marrazza, A. Kaushik and S. Kumar, *Adv. Colloid Interface Sci.*, 2023, **322**, 103024.

43 X. Xu, W. Xu, L. Zhang, G. Liu, X. Wang, W. Zhong and Y. Du, *Sep. Purif. Technol.*, 2021, **278**, 119569.

44 G. E. P. Box and K. B. Wilson, in *Breakthroughs in statistics: methodology and distribution*, Springer, 1992, pp. 270–310.

45 G. E. P. Box and D. W. Behnken, *Technometrics*, 1960, **2**, 455–475.

46 E. H. Ibrahim, N. A. Tajuddin, H. A. A. Hamid, S. H. Saleh, N. M. Hadzir, R. Osman, M. Saaid and N. Hamzah, *Malaysian J. Chem.*, 2022, **24**, 97–109.

47 M. A. Bezerra, R. E. Santelli, E. P. Oliveira, L. S. Villar and L. A. Escaleira, *Talanta*, 2008, **76**, 965–977.

48 F. W. L. Silva, L. L. Name, D. Y. Tiba, B. F. Braz, R. E. Santelli, T. C. Canevari and F. H. Cincotto, *Talanta*, 2024, **266**, 125075.

49 G. Derringer and R. Suich, *J. Qual. Technol.*, 1980, **12**, 214–219.

50 N. T. Shelke and B. R. Karche, *J. Alloys Compd.*, 2015, **653**, 298–303.

51 S. Ratha and C. S. Rout, *ACS Appl. Mater. Interfaces*, 2013, **5**, 11427–11433.

52 S. Keerthana, A. Rajapriya, S. Amirthapandian, C. Viswanathan and N. Ponpandian, *Colloids Surfaces A Physicochem. Eng. Asp.*, 2021, **618**, 126452.

53 R. Shokoohi, D. Nematollahi, M. R. Samarghandi, G. Azarian and Z. Latifi, *Environ. Technol. Innov.*, 2020, **18**, 100711.

54 N. AttariKhasraghi, K. Zare, A. Mehrizad, N. Modirshahla and M. A. Behnajady, *J. Inorg. Organomet. Polym. Mater.*, 2021, **31**, 3164–3174.

55 M. Abrishamkar, *Electroanalysis*, 2021, **33**, 1866–1870.

56 M. Staiger, R. Gillen, N. Scheuschner, O. Ochedowski, F. Kampmann, M. Schleberger, C. Thomsen and J. Maultzsch, *Phys. Rev. B - Condens. Matter Mater.*

Phys., 2015, **91**, 1–8.

View Article Online
DOI: 10.1039/D6SU00059B

57 A. Berkdemir, H. R. Gutiérrez, A. R. Botello-Méndez, N. Perea-López, A. L. Elías, C. I. Chia, B. Wang, V. H. Crespi, F. López-Urías, J. C. Charlier, H. Terrones and M. Terrones, *Sci. Rep.*, 2013, **3**, 1–8.

58 X. H. Wang, J. Q. Ning, C. C. Zheng, B. R. Zhu, L. Xie, H. S. Wu and S. J. Xu, *J. Mater. Chem. C*, 2015, **3**, 2589–2592.

59 H. Dang, L. Chen, L. Chen, M. Yuan, Z. Yan and M. Li, *Mater. Lett.*, 2019, **254**, 42–45.

60 S. Cao, T. Liu, W. Zeng, S. Hussain, X. Peng and F. Pan, *J. Mater. Sci. Mater. Electron.*, 2014, **25**, 4300–4305.

61 S. Deng and V. Berry, *Mater. Today*, 2016, **19**, 197–212.

62 Y. Huang, Y. Jiang, Z. Ma, Y. Zhang, X. Zheng, X. Yan, X. Deng, W. Xiao and H. Tang, *Nanomaterials*, 2019, **9**, 469.

63 Y. Liu, W. Wang, Y. Wang and X. Peng, *Nano Energy*, 2014, **7**, 25–32.

64 Z. Wei, Y. Zhang, M. Li, C. Shu and D. Deng, *J. Energy Storage*, 2024, **81**, 110115.

65 W. P. Wicaksono, H. Dang, S. Lee and J. Choo, *Appl. Surf. Sci.*, 2024, **649**, 159163.

66 M. Hashemi, F. Rahimi, S. Abolghasemi and A. Nasiri, *Environ. Technol. Innov.*, 2025, **37**, 103914.

67 M. R. Majidi, K. Asadpour-Zeynali and B. Hafezi, *Anal. Methods*, 2011, **3**, 646–652.

68 Y. Salimonnafs, B. MemarMaher, L. Amirkhani and F. Derakhshanfard, *Int. J. Polym. Mater. Polym. Biomater.*, 2023, **72**, 366–375.

69 M. M. Aleksić, N. Lijeskić, J. Pantić and V. P. Kapetanović, *Facta Univ. Physics, Chem. Technol.*, 2013, **11**, 55–66.

70 P. R. Dalmasso, M. L. Pedano and G. A. Rivas, 2012, DOI: 10.1016/j.snb.2012.07.087.

71 I. Taverniers, M. De Loose and E. Van Bockstaele, *TrAC Trends Anal. Chem.*, 2004, **23**, 535–552.

View Article Online
DOI: 10.1039/D6SU00059B

Data Availability

The data that support the findings of this study are available from the corresponding author upon request.